Geometric Effects on the Amplification of First Mode Instability Waves

A THESIS
SUBMITTED TO THE FACULTY OF THE GRADUATE SCHOOL
OF THE UNIVERSITY OF MINNESOTA
BY

Lindsay Christine Kirk

IN PARTIAL FULFILLMENT OF THE REQUIREMENTS
FOR THE DEGREE OF
MASTER OF SCIENCE

Graham V. Candler, Advisor

May, 2013

Acknowledgements

I would like to thank my advisor for his support of and guidance during this work. I would also like to thank Dr. Heath Johnson for the use of his automated grid generation code and assistance with the STABL boundary layer stability software, as well as Dr. Travis Drayna for an introduction to the DAKOTA optimization software and access to his driver routine to start optimizations for this work. Finally, thanks to Roger Greenwood at Purdue University, who is working on measuring first mode instabilities in a ground test facility, for discussions that have been instrumental in understanding some of the computational results in this research.

This work was sponsored in part by the NASA Johnson Space Center Academic Fellowship, by the Air Force Office of Scientific Research under grant FA9550-12-1-0064, and by the Department of Defense National Security Science & Engineering Faculty Fellowship. The views and conclusions contained herein are those of the author and should not be interpreted as necessarily representing the official policies or endorsements, either expressed or implied, of the sponsors or the U.S. Government.

Dedication

To my parents, my husband, and my kids for their love, support, and motivation when I needed it most.

Abstract

The effects of geometric changes on the amplification of first mode instability waves in an external supersonic boundary layer were investigated using numerical techniques. Boundary layer stability was analyzed at Mach 6 conditions similar to freestream conditions obtained in quiet ground test facilities so that results obtained in this study may be applied to future test article design to measure first mode instability waves. First, geometric parameters such as nose radius, cone half angle, vehicle length, and surface curvature for an axisymmetric cone geometry were examined separately to determine the individual effects on the first mode amplification. The DAKOTA optimization software package was then used to optimize the geometry to maximize the amplification of waves at first mode frequencies and to minimize the amplification of the waves at second mode frequencies, as computed by the 2D STABL hypersonic boundary layer stability analysis tool. This was accomplished by allowing all geometric parameters in the sensitivity study to vary to produce a shape optimized to maximize the amplification of first mode instability waves while minimizing the amplification of second mode instability waves. During this process, boundary layer edge properties were recorded to investigate any correlations. Results of the sensitivity analysis indicate that an axisymmetric cone with a sharp nose or an axisymmetric cone with a high degree of concave curvature under the Mach 6 freestream conditions used here will cause the largest amplification of first mode instability waves.

Contents

List of Tables

List of Figures

Chapter 1

Introduction

1.1 Hypersonic Boundary Layer Stability and Transition

Predicting the location and method by which the boundary layer on a hypersonic vehicle will transition from laminar flow to turbulent flow is a difficult problem that many researchers have spent careers trying to solve. Boundary layer transition is a complex process that can be governed by fluctuations in freestream properties such as density and temperature, vehicle surface roughness and curvature, boundary layer properties, and many other geometric and flow phenomena. While many advances have been made in determining the characteristics of a boundary layer and its stability, none yet have the capability to predict transition as a stand-alone method.[1] Understanding the transition process and the ability to predict when and where transition may occur on a vehicle during hypersonic flight is important to the vehicle performance and controlability as well as the design of the thermal protection system (TPS). The transition process causes dramatic changes in the skin friction at the surface, which will change the drag acting on the vehicle. These changes in the skin friction, if asymmetric, can also impart moments on the vehicle that must be accounted for in the design of the control systems. Transition from laminar to turbulent flow at supersonic and hypersonic speeds can cause the surface heat transfer to increase by a factor of three to five times. The TPS must be designed to accommodate this increase to protect the structural components as well as the payload. However, the mass of the vehicle is a common design constraint, so the TPS mass must be balanced with the mass of the other components to meet design

requirements, so prediction accuracy is very important.

Many flight vehicles for defense applications are slender cones that fly at conditions that produce high edge Mach numbers (above ≈ 5), and at these conditions, transition to turbulence is generally dominated by second mode instabilities. For this reason, much of the research on boundary layer transition and boundary layer instability mechanisms has been focused on second mode instabilities. Measurements of second mode instability waves have been made in several ground test facilities, which include measurements in quiet flow by Alba, et al.[2] in the Boeing/AFOSR Mach 6 Quiet Tunnel and conventional flow in short duration facilities by Wadhams, et al.[3],[4] in the CUBRC LENS-II reflected shock tunnel and Berridge, et al.[5] in the Arnold Engineering Development Center Tunnel 9 and the Mach 6 and Mach 10 Tunnels at Langley Research Center.

In contrast to the slender cones used in defense applications, many exploration vehicles are blunt capsule geometries that reenter the atmosphere at conditions that produce low edge Mach numbers. These vehicles usually have limits on the deceleration loading due to sensitive science payloads or crewed missions. These geometries are believed to transition due to first mode instabilities, but there is a dearth of research on the topic. First mode instabilities have proven much harder to measure and confirm in ground test facilities, so much work is left to be done to understand the behavior of first mode instabilities.

1.2 Overview and Objectives of Current Work

Determining the effects of geometric changes on the amplification of first mode instabilities in a hypersonic boundary layer can lead to a better understanding of transition due to first mode instabilities and more intelligent design of test articles and flight vehicles. In contrast to slender cones with high edge Mach numbers where transition is generally dominated by second mode and cross-flow instabilities, many blunt vehicles such as reentry capsules and lifting bodies, where the highest lift-to-drag ratios are achieved at high angles of attack, will likely transition on the heat shield or wind side of the vehicle due to first mode instabilities. This is due to the thicker boundary layers that develop and the low edge Mach numbers, which can result from nose bluntness of a vehicle or by the flow being slowed through an oblique shock.

The work presented here examines the effects of geometric changes on the amplification of first mode instability waves. For fixed freestream conditions and wall temperature, the geometric parameters defining an axisymmetric cone are varied to determine how changes in the geometry affect the growth of first mode instabilities. In this study, an axisymmetric cone geometry was chose for simplicity and the opportunity to use two-dimensional analysis tools. First, a sensitivity analysis was performed on the effects of varying the nose radius, cone length, cone half angle, degree of convex curvature, and degree of concave curvature (each parameter was varied independently and all other variables were held constant). Next, all the geometric parameters were allowed to vary simultaneously with the aim to deduce an 'optimal' geometry that produces the maximum amplification of first mode waves while simultaneously minimizing the amplification of second mode waves. Since oblique first mode waves are known to be most unstable[6], the boundary layer stability analyses in this study were done at wave frequencies around the predicted first mode frequency as well as at a broad range of oblique wave angles to determine the amplification of the first mode waves. First mode instability waves are seen most often in flows with low edge Mach numbers: for this reason, the edge Mach number and other boundary layer properties were recorded for each geometry to determine any correlations between the first mode stability and the boundary layer properties.

Chapter 2

Background

2.1 First Mode Instability Waves

In supersonic and hypersonic flows, the first mode instabilities that can develop in a boundary layer are viscous instabilities akin to the Tollmein-Schlichting waves seen in incompressible flows. The second mode instabilities, which are commonly associated with hypersonic boundary layer transition, are inviscid instabilities that result from a generalized inflection point where the gradient of the product of density and vorticity goes to zero.[7] Whereas second mode instabilities are most unstable to two dimensional disturbances aligned with the stream-wise flow direction, the most unstable first mode disturbances (at supersonic and hypersonic conditions) are three-dimensional oblique waves.[6] First mode instabilities are found in flows with low Mach numbers (usually less than 5) at the edge of the boundary layer, but second mode instabilities are dominant in flows with higher edge Mach numbers.[8] This is due to the viscous instability becoming weaker as the freestream Mach number increases and the inviscid instability increasingly dominating the boundary layer stability characteristics. Second mode disturbances consist of higher frequency waves that are trapped and grow within the boundary layer and roughly scale with the boundary layer thickness. Perturbations associated with the first mode have longer wavelengths, lower amplitudes, and are harder to predict.

Both first and second mode waves are strongly affected by the wall temperature. First mode waves have been shown to be stabilized by wall cooling and destabilized by wall heating.[7] The opposite is true for second mode instability waves, so conditions

which stabilize one instability mechanism may destabilize the other. Studies have shown that decreasing the wall-to-total temperature ratio can increase the amplification of second mode instabilities and stabilize the first mode instabilities; high speed, short duration ground test facilities typically operate at low wall-to-total temperature ratios, which makes it difficult to measure first mode instabilities. Blanchard and Selby[9] measured the growth of some low frequency disturbances on an axisymmetric flared cone with a cooled wall under Mach 6 conditions in a quiet tunnel, but it was not confirmed that those disturbances correspond to the first mode.

2.2 Parabolized Stability Equations and Boundary Layer Stability Analysis

Linear stability theory (LST) and the linear parabolized stability equations (PSE) methods can be used to compute boundary layer stability characteristics. These methods use a laminar basic state and assume small perturbations in flow properties for pressure, density, temperature, and three components of velocity, shown in Equation 2.1 where the capitalized or tilde variables denote basic state parameters and primed variables denote the fluctuating portion of the flow parameter.

$$\begin{aligned} p &= P + p' \\ \rho &= \tilde{\rho} + \rho' \\ T &= \tilde{T} + T' \\ \mathbf{u} &= \mathbf{U} + \mathbf{u}' \end{aligned} \tag{2.1}$$

The perturbed variables are then substituted into the axisymmetric Navier-Stokes equations and the steady state equations are subtracted to obtain the disturbance equations.

LST methods model the growth and decay of these small disturbances as normal modes, which, in flows where spanwise variation is negligible, reduce to

$$\mathbf{q'}\,(x, y, t) = \mathbf{q}\,(y)\, exp\,[i\,(\alpha x - \omega t)] \tag{2.2}$$

where **q'** is a vector of flow variables and **q** is a vector of shape functions. Substitution of these normal modes into the disturbance equations results in an eigenvalue problem with homogeneous boundary conditions that can be solved for the spatial growth rate of the disturbances in the x directions, $-\alpha_i$.

Assuming all perturbations are small allows for the non-linear terms to be neglected, and with the additional assumption of a locally parallel flow, the perturbations in the PSE method can be modeled as a fast oscillatory wave and a slowly varying shape function. This allows for modification to the normal modes used in LST by using a phase function, and the eigenvalue problem for basic state flows without a spanwise variation reduces to

$$\left(\mathbf{L} + \epsilon\mathbf{L}'\right)\mathbf{q} + \epsilon\mathbf{M}_1\frac{\partial\mathbf{q}}{\partial\xi} = \mathbf{r} \tag{2.3}$$

where $\mathbf{q}$ is the vector of flow variables, $\mathbf{L}$, $\mathbf{L}'$, and $\mathbf{M}_1$ are operators in the off-body direction only, ξ allows for slow variations in the streamwise direction, and $\mathbf{r}$ on the right hand side includes the non-linear terms. A detailed derivation of the PSE methodology can be found in *Parabolized Stability Equations* by Thorwald Herbert [10].

Modeling the disturbances in this way gives the spatial variation of a specific fixed disturbance frequency, ω, along the body. The growth rate of each disturbance is defined by

$$\sigma = -Im\left(\alpha\right) + \frac{1}{2E}\frac{dE}{ds} \tag{2.4}$$

where α is the complex stream-wise wave number and E, the disturbance kinetic energy, is

$$E = \int_n \bar{\rho}\left(|u'|^2 + |v'|^2 + |w'|^2\right)dn \tag{2.5}$$

Above, $\bar{\rho}$ is the mean flow density and u', v', and w' are the complex fluctuating velocity components, and the integration is performed in the body normal direction, n.

The amplification of each disturbance is then integrated by

$$N(\omega, s) = \int_{s_0}^{s} \sigma ds \tag{2.6}$$

to determine the integrated growth rate of unstable disturbances, or N factor, in the boundary layer. In the above equation, s is the distance along the body, s_0 is the point where the disturbance first becomes unstable, and σ is the disturbance growth rate defined in Equation 2.4. More information on the implementation of this method in the PSE-Chem software, which is part of the STABL (Stability and Transition Analysis for Hypersonic Boundary Layers) software suite, used for analysis in this work can be found in Johnson and Candler[11] and Johnson[12]. The STABL software suite uses the boundary layer properties provided in the provided mean flow solution to solve these equations to obtain the growth and decay of disturbances over a range of frequencies to determine the stability of the boundary layer. This process will be described further in Section 3.1.3.

Chapter 3

Methodology

The effects of geometry on the amplification of first mode instabilities were investigated in two parts. In both cases, the geometry was an axisymmetric cone with no angle of attack so the study could be completed with 2D analysis tools for simplicity. The freestream conditions for this study were chosen to be supersonic, but at conditions where the edge Mach number would be low enough, below ≈5, for first mode instabilities to be amplified and cause transition. First, the sensitivity of the first mode amplification to changes in specific geometric parameters was examined to gain an understanding of the effects of each parameter. Next, a combination of tools was used to allow all the geometric parameters to vary simultaneously to optimize a geometry where the effects of second mode instabilities were minimized, first mode instabilities were amplified, and first mode instabilities could grow to be large enough to expect transition. This optimization process is similar to the work performed by Johnson, et al.[13] investigating the amplification of second mode instabilities on 2D and 3D geometries.

It is hypothesized that first mode N factors of ≈5-6 are required to cause transition due to first mode instabilities in a conventional ground test facility, and research has shown that the maximum amplification of first mode waves is typically seen at oblique angles. Therefore, in the ensuing analysis, examination of oblique wave sensitivity is expected to be critical.

3.1 Geometric Sensitivities

The amplification of first mode instabilities due to changes in geometry was determined by varying the nose radius, body length, cone half angle, concave curvature, or convex curvature of an axisymmetric geometry individually. In each case, the nose of the cone geometry was made spherical, and all other parameters were held constant while one parameter was changed. The baseline geometry was a 10° half angle cone, 1 meter long with no curvature and a nose radius of 5.0 millimeters. Figure 3.1 shows the parameters that were varied in the sensitivity analysis, and Table 3.1 shows the ranges over which each parameter was allowed to vary.

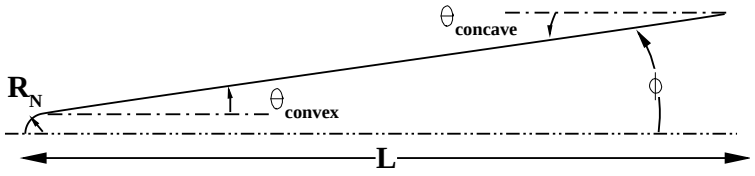

Figure 3.1: Parameters Varied in Sensitivity Analysis

Table 3.1: Geometric Sensitivity Parameters and Ranges Investigated

Geometric Parameter	Minimum	Maximum
Nose Radius [mm]	1.0	100.0
Length [m]	0.3	1.5
Half Angle [°]	2.0	45.0
Concave Curvature [°]	6.0	26.0
Convex Curvature [°]	10.0	70.0

3.1.1 Grid Generation

For each configuration, a two-dimensional computational grid was generated based on the specified geometric parameters. These geometric variables defined the surface of the geometry, and the outer boundary of the grid was specified far away from the surface to contain the entire shock for a variety of geometric shapes. The grid used 600 points per meter of length in the stream-wise direction with 90 of those points resolving the nose of the body and 500 points in the off-body direction. This allowed for the grid resolution to stay approximately the same as the sensitivity of the first mode instability growth

rate to the vehicle length was examined. When the grid outer boundary was tailored to the shock location, grid points were also clustered near the wall to better resolve the boundary layer. A y^+ value less than unity in the first off-body cell was used to ensure ≈200 points were clustered in the boundary layer.

3.1.2 CFD Mean Flow Solution

Laminar mean flow solutions for the boundary layer stability analysis were then computed with the US3D finite volume, Navier-Stokes code developed at the University of Minnesota.[14] Solutions were computed with non-reacting air at the Mach 6.0 conditions shown in Table 3.2 since, at these low total temperatures ($T_0 = 430K$), chemistry has a negligible effect on the solution. These conditions produce a wall-to-total temperature ratio of 0.69. A DPLR (Data-Parallel Line Relaxation) method was used with Steger-Warming fluxes to produce a second-order accurate mean flow solution.

Table 3.2: Freestream Conditions for Mean Flow Calculations

Re/m	U_∞ [m/s]	T_∞ [K]	ρ_∞ [kg/m^3]	T_w [K]	α [deg]
1.93x10^6	871.0	52.44	0.0436	300.0	0.0

The mean flow solutions needed for the boundary layer stability analysis were computed with US3D and were obtained by first solving the equations on the untailored mesh with coarse wall spacing. Once the solution was converged, a grid tailoring algorithm was used to tailor the outer boundary of the grid to the shock location and reduce the wall spacing to better resolve the boundary layer. This process clusters approximately 200 points in the boundary layer to provide enough points to accurately compute the higher order derivatives in the boundary layer that are required for the stability analysis. Figure 3.2 shows the mean flow solution for a representative geometry with the untailored grid on top and the shock-tailored grid on the bottom. The shock-tailored grid was then used for the boundary layer stability analysis.

3.1.3 Boundary Layer Stability Analysis

The boundary layer stability analysis was completed using the two-dimensional stability modeling software, STABL (Stability and Transition Analysis for Hypersonic Boundary Layers), which employs the LST and linear PSE methods described in Section 2.2 in

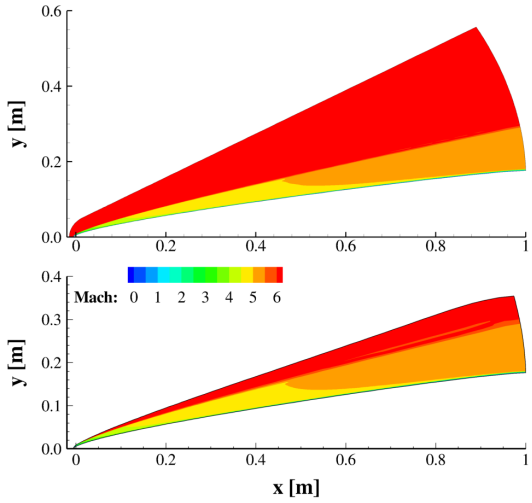

Figure 3.2: Untailored (top) and Shock-tailored (bottom) Mean Flow Solutions

"Hypersonic Boundary Layer Stability Analysis Using PSE-Chem"[11]. The STABL software uses the boundary layer properties provided in the mean flow solution to compute the approximate first and second mode disturbance frequencies along the body. The user then specifies matrices of test points along the body spanning the predicted frequencies for analysis of the boundary layer stability. Since the location where a disturbance first becomes unstable, s_0 in Equation 2.6, is unknown, the test points specified in STABL are used as initial guesses. Then the growth or decay of a disturbance that initially becomes unstable at the specified stream-wise location, frequency, and oblique wave angle is integrated down the length of the body to compute the N factor. For this study, test points were clustered along the body around the first mode frequencies predicted by STABL. In addition to the test points at the first mode frequencies, test points were added at a broad range of oblique wave angles to analyze the amplification of first mode waves with oblique angles.

Once the stability analysis was completed, the maximum N factor and the corresponding oblique wave angle were recorded, as well as several boundary layer properties, including the boundary layer thickness, the temperature at the edge of the boundary layer, and the Mach number at the edge of the boundary layer. These data were recorded and then analyzed to determine the sensitivities of the first mode N factors to changes in individual geometric parameters.

3.2 Geometric Optimization

The optimization study was completed using the DAKOTA (Design Analysis Kit for Optimization and Terascale Applications) optimization package developed at Sandia National Laboratories.[15] The DAKOTA package includes many options for optimization algorithms. The user provides a routine that defines the parameters being optimized and an objective function that DAKOTA uses in the optimization process. In this study, a Perl driver routine was written to orchestrate the process of evaluating the objective function for a given geometric parameterization, which included parameterizing the geometry, generating the grid, computing the mean flow solution, performing the boundary layer stability analysis, and computing the objective function to be optimized. Figure 3.3 shows the optimization control loop.

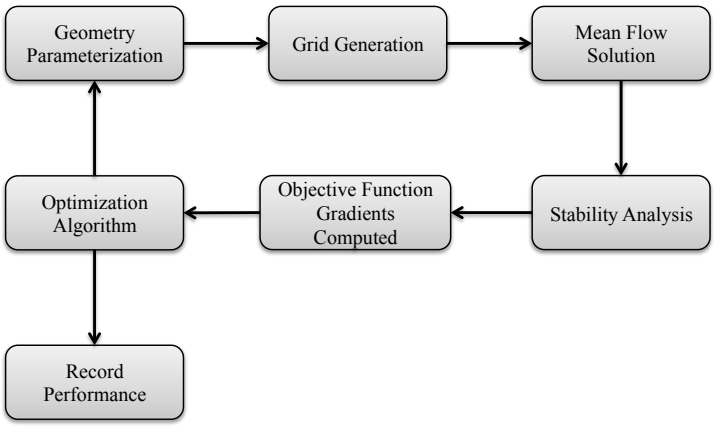

Figure 3.3: Optimization Control Loop

As with the sensitivity study, this study was restricted to axisymmetric geometries at 0° angle of attack for simplicity. The geometries in this case, however, were parameterized as shown in Figure 3.4 to allow DAKOTA to change the geometry during the optimization process. Two control points were specified, CP_1 near the nose and CP_4 near the tail. At each of those control points, the radial distance to another point (CP_2 and CP_3, respectively) and the angle between the horizontal and the vector defined by those two points (θ_1 and θ_2, respectively) were specified. Figure 3.4(a) shows the

relative locations of the control points for a representative geometry. A Bezier curve between the nose control point and the tail control point, restricted by the vectors and angles, was used to define the shape of the body. Two nose radii, $R_{N,a}$ and $R_{N,b}$ seen in Figure 3.4(b), could be specified to define an elliptical nose geometry. A spherical nose geometry would result if $R_{N,a}$ and $R_{N,b}$ were equal, and the geometries in the sensitivity analysis and optimizations for this study were restricted to spherical nose geometries for simplicity. The length of the body and the base radius were also specified to determine the equivalent of the half-angle for a cone geometry. Each of these parameters was specified as an input to the grid generation process and was also used as a sensitivity variable in the optimization process. DAKOTA would then automatically vary each of these parameters to perform a gradient-based optimization.

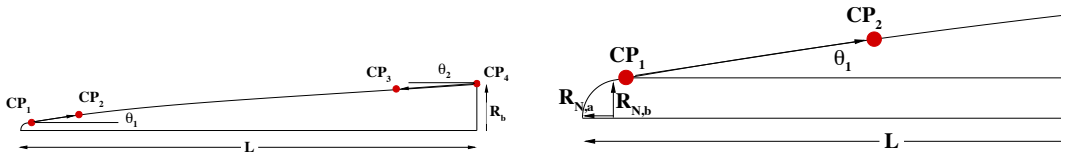

(a) Control Point Definitions

(b) Nose Radius Definitions

Figure 3.4: Geometry Parameterization

Following the geometry parameterization, the grid generation, mean flow computations, and boundary layer stability analysis were performed in the same ways described in Section 3.1. The initial geometry parameterization was specified by the user, and subsequent geometry shapes were determined by gradients in the objective function with respect to each of the sensitivity variables (nose radius, body length, etc.). The objective function used for this analysis was a combination of the maximum first mode N factor computed in a boundary layer stability analysis with first mode frequencies and oblique wave angles and the maximum second mode N factor computed in a boundary layer stability analysis with second mode frequencies but no oblique waves. This required that two separate stability analyses be completed to get the two different N factors. The objective function used by DAKOTA was then defined by

$$OF = \frac{\left(N_{max,1^{st}mode}\right)^2}{N_{max,2^{nd}mode}} \tag{3.1}$$

and the objective function was maximized during the optimization process. This maximized the first mode amplification while minimizing the second mode amplification to preclude second mode transition, but weighted the maximization of first mode amplification as more important than the minimization of second mode amplification.

To determine the gradient in the objective function with respect to the sensitivity variables, each of the sensitivity variables was perturbed by a small amount and the grid, mean flow, and stability analyses were performed with the perturbed geometry. The resulting maximum N factors were found and the objective function was recomputed. These finite differenced approximate partial derivatives were computed based on the small changes in geometry, and the DAKOTA optimization software used the resulting approximate gradients in the optimization algorithms to determine the geometry parameterization of the next design iteration. The geometry optimization was completed when the objective function converged to within a specified tolerance.

The purpose of the optimization using the DAKOTA software package was to gain an understanding of the geometric features which may cause the amplification of first mode instabilities with oblique wave angles. First mode instabilities have been seen to be most amplified in supersonic flows where the Mach number at the edge of the boundary layer is low. Since the edge Mach number can be reduced through nose bluntness or through a strong oblique shock, the optimization procedure was performed in two pieces. One optimization was performed restricting the half angle and nose radius to examine slender bodies with smaller nose radii where the edge Mach number would be reduced through the presence of an oblique shock. The second optimization allowed the nose radius and the cone half angle to be larger to reduce the edge Mach number with nose bluntness. The composite geometries optimized to amplify first mode instabilities and stabilize second mode instabilities, as well as the results from each of the individual sensitivity variables, could be used as guidelines for future test article or flight vehicle design.

Chapter 4

Results

Presented here are the results of the geometric sensitivity analysis followed by the results of the geometric optimization. In the geometric sensitivity analysis, the effects of changes in each geometric parameter on the boundary layer stability were analyzed individually by holding all other geometric parameters constant. Then, in the optimization, all geometric parameters were allowed to vary to determine the geometry that would maximize the amplification of the first mode instabilities. Two optimizations were performed: one which would limit the geometry to a slender cone to lower the edge Mach number through an oblique shock, and one which would limit the geometry to a blunt cone with a larger half angle to lower the edge Mach number through bluntness.

4.1 Sensitivity Analysis

The maximum first mode N factor was computed for axisymmetric cones where each of the geometric parameters was varied over a range of values to determine how each parameter affects the growth of first mode waves. The Mach number at the edge of the boundary layer at the aft end of the geometry was also recorded to see if any trends could be seen between the edge Mach number and the maximum first mode N factors. The baseline geometry was a 1.0 meter long, 10° half-angle cone with no curvature and a spherical nose with a 5.0 millimeter radius. The nose radius, body length, cone half-angle, degree of convex curvature, and degree of concave curvature were all examined in the sensitivity analysis and the variations can be found in Table 4.1. The cone half angle was defined by the base radius and the geometry length, $\phi = atan(R_b/L)$, and the degree of convex and concave curvature were related to the values of θ_1 and θ_2, respectively, as defined in Section 3.2.

The maximum first mode N factor was determined from the integration of the disturbance growth rate along the length of the body for each of the test points in the STABL analysis test matrix. Only disturbances at first mode frequencies with an oblique wave angle greater than 5° were considered. For each configuration, the maximum first mode N factor curve was computed as the maximum of all the first mode N factors at each stream-wise location along the body. An example of this can be seen in Figure 4.1. In examining the datasets for each of the geometric parameters, the maximum first mode N factor was recorded along with the edge Mach number at the aft end of the geometry, as it was assumed that this would give the maximum edge Mach number. The trends seen in the edge Mach number and maximum first mode N factor were also supplemented with an examination of other boundary layer properties for further understanding of the behavior of first mode instability waves. For each of the sensitivity parameters, the boundary layer thickness, momentum thickness, edge temperature, and momentum thickness Reynolds number were extracted along the length of the body and compared to the first mode N factors computed along the body in the stability analysis.

Table 4.1: Variation of Geometric Parameters for Sensitivity Analysis

R_N [mm]	L [m]	ϕ [°]	$\theta_{concave}$ [°]	θ_{convex} [°]
1.0	1.00	10.0	0.0	0.0
3.0	1.00	10.0	0.0	0.0
5.0	1.00	10.0	0.0	0.0
10.0	1.00	10.0	0.0	0.0
30.0	1.00	10.0	0.0	0.0
50.0	1.00	10.0	0.0	0.0
100.0	1.00	10.0	0.0	0.0
5.0	0.30	10.0	0.0	0.0
5.0	0.45	10.0	0.0	0.0
5.0	0.60	10.0	0.0	0.0
5.0	0.75	10.0	0.0	0.0
5.0	0.90	10.0	0.0	0.0
5.0	1.05	10.0	0.0	0.0
5.0	1.20	10.0	0.0	0.0
5.0	1.35	10.0	0.0	0.0
5.0	1.50	10.0	0.0	0.0
5.0	1.00	2.0	0.0	0.0
5.0	1.00	5.0	0.0	0.0
5.0	1.00	10.0	0.0	0.0
5.0	1.00	20.0	0.0	0.0
5.0	1.00	30.0	0.0	0.0
5.0	1.00	40.0	0.0	0.0
5.0	1.00	45.0	0.0	0.0
5.0	1.00	10.0	6.0	0.0
5.0	1.00	10.0	10.0	0.0
5.0	1.00	10.0	14.0	0.0
5.0	1.00	10.0	18.0	0.0
5.0	1.00	10.0	22.0	0.0
5.0	1.00	10.0	26.0	0.0
5.0	1.00	10.0	0.0	10.0
5.0	1.00	10.0	0.0	20.0
5.0	1.00	10.0	0.0	30.0
5.0	1.00	10.0	0.0	40.0
5.0	1.00	10.0	0.0	50.0
5.0	1.00	10.0	0.0	60.0
5.0	1.00	10.0	0.0	70.0

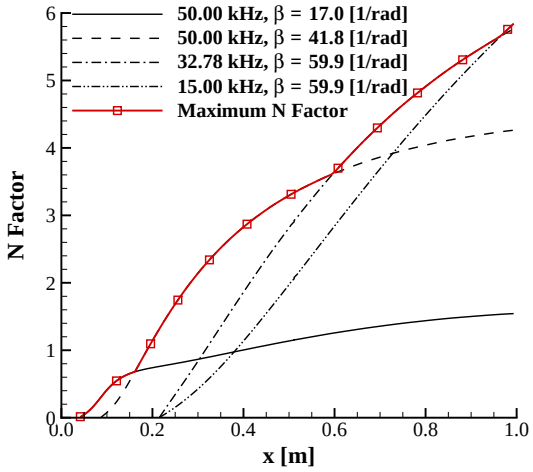

Figure 4.1: Sample Maximum First Mode N Factor Curve

4.1.1 Effect of Nose Radius

First, the effects of changes in the nose radius were examined. Figure 4.2(a) shows the shape of the nose for each of the cases. In Figure 4.2(b), the edge Mach number along the body decreases as the nose radius is increased. The maximum first mode N factors along the length of the body computed from the stability analysis are shown for each of the nose radii in Figure 4.2(c), and it can be seen that for the geometries with a smaller nose radius, the maximum first mode N factors occur towards the aft end of the vehicle. In contrast, as the nose radius is increased, the maximum first mode N factors for a given geometry appear closer to the nose. This occurs because the method that lowers the edge Mach number changes from an oblique shock to nose bluntness. Figure 4.2(d) shows the relationship between the maximum first mode N factor from the stability analysis and the edge Mach number at the aft end of the geometry. The trend in increasing nose radius is noted with the arrow, and all points follow this trend with the exception of the largest nose radius, which is labeled on the plot. The results show that as the nose radius is increased, the edge Mach number at the aft end of the vehicle decreases along with the maximum first mode N factor. The maximum first mode N factor of 5.9 for this sensitivity analysis occurs at the smallest nose radius of

1 mm, which also corresponds to the geometry where the edge Mach number is the largest and the edge temperature is the smallest. This inverse relationship between the edge temperature and edge Mach number is to be expected in an adiabatic flow, but this also results in the largest ratio of wall-to-edge temperatures ($T_W/T_e = 2.4$) seen in this part of the sensitivity analysis. It should be noted that some of the properties extracted appear to have jagged distributions along the body. This results from the method used to determine the edge of the boundary layer, which does not use any smoothing techniques when the edge of the boundary layer lies between cells.

Examining changes in the boundary layer properties as the nose radius changes, seen in Figure 4.3, the boundary layer thickness is greatest (≈ 5.5 mm) when the nose radius is large, and the momentum thickness Reynolds number, Re_θ, distribution along the body flattens out as the nose radius increases. This may also result from the change in cone half angle when the nose radius is increased and the base radius remains the same. A future analysis should work to isolate these effects. When the nose radius is small, the edge Mach number is reduced through an oblique shock, but as the nose radius increases, the flow is slowed through nose bluntness and the boundary layer stability characteristics change causing a steep drop in the maximum first mode N factors seen in the stability analysis.

It should be noted, however, that changing the nose radius in this way without accounting for the change in half angle as the nose radius is increased is likely providing results that are not completely isolating the effects of changes in the nose radius. A more independent analysis would adjust the base radius of the cone to account for the increasing nose radius to maintain a constant half angle.

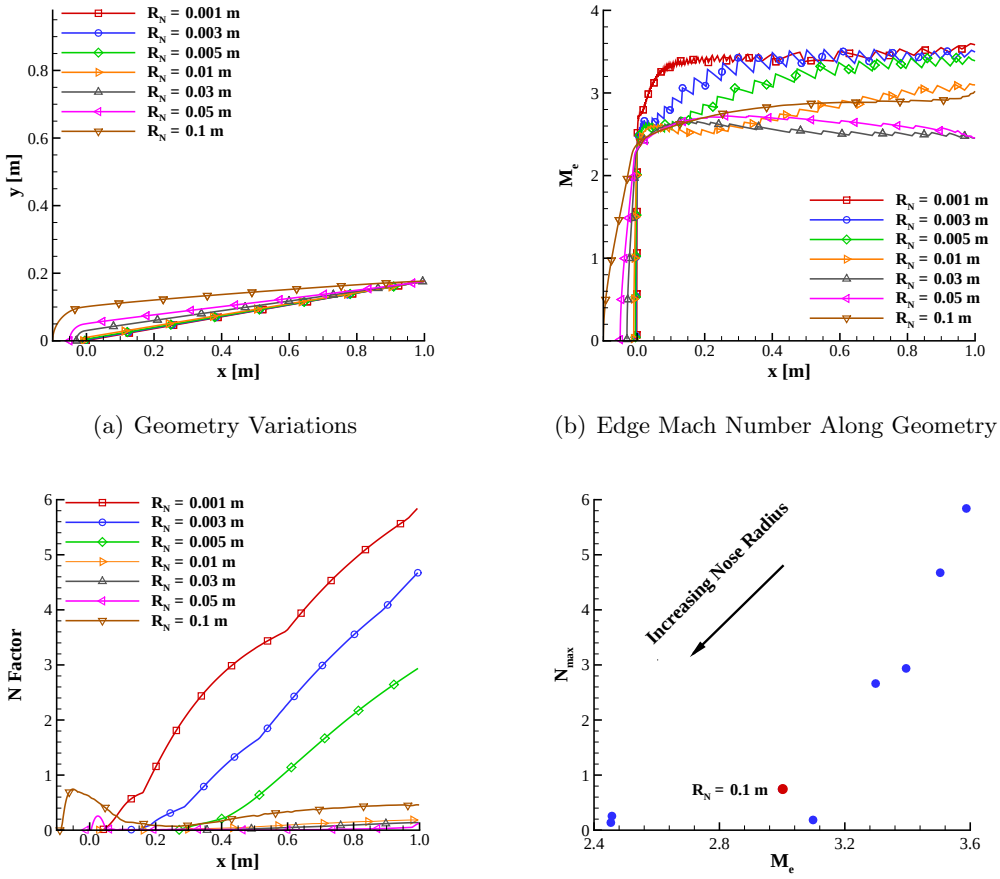

(a) Geometry Variations

(b) Edge Mach Number Along Geometry

(c) Maximum First Mode N Factors Along Geometry

(d) Trend in Maximum First Mode N Factors with Edge Mach Number at Aft End of Geometry

Figure 4.2: Nose Radius Sensitivities

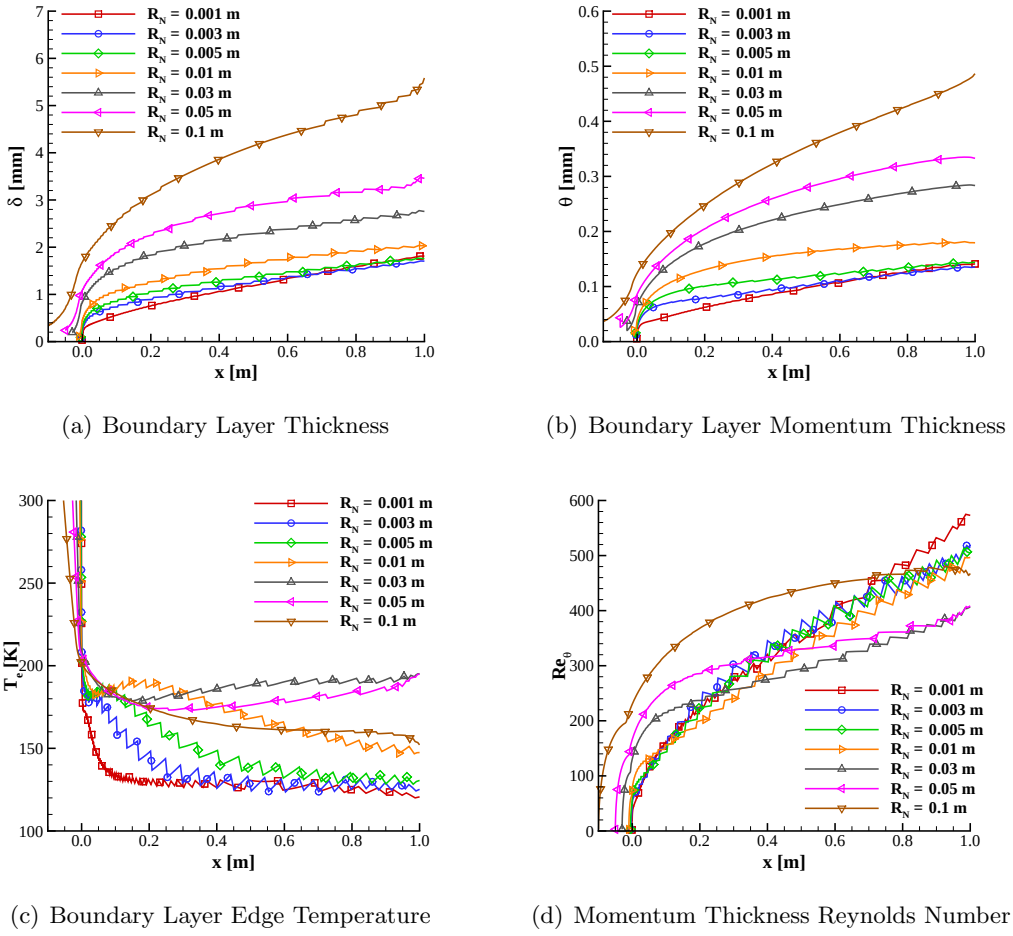

(a) Boundary Layer Thickness

(b) Boundary Layer Momentum Thickness

(c) Boundary Layer Edge Temperature

(d) Momentum Thickness Reynolds Number

Figure 4.3: Changes in Maximum First Mode N Factor with Boundary Layer Properties at Aft End of Vehicle for Changes in Nose Radius

4.1.2 Effect of Vehicle Length

Sensitivities to changes in the length of the vehicle were examined next. Figure 4.4(a) shows the lengths of each geometry denoted by the vertical lines at the end of each of the geometries studied. The results showed expected trends in the maximum first mode N factor as well as edge Mach number at the aft end of the geometry. As the vehicle length increases, the edge Mach number at the aft of the vehicle approaches a constant value and the disturbances are allowed a longer distance to amplify. As a result, the maximum first mode N factors increase as the length of the body increases and reach a maximum of 4.5 and the boundary layer velocity thickness reaches a maximum of 2.1 mm for the longest vehicle length studied. In Figure 4.4(c), the maximum first mode N factors increase as the vehicle length is increased, but the onset of the amplification is delayed in the two longest geometries. This is likely due to differences in the stability test matrix resolution between those two cases and the others in this sensitivity analysis since there are not any significant differences in the boundary layer properties. Figure 4.5 shows how the boundary layer properties for each geometry lay on top of each other since nothing is changing near the nose of each of the geometries that would influence the boundary layer properties or stability downstream.

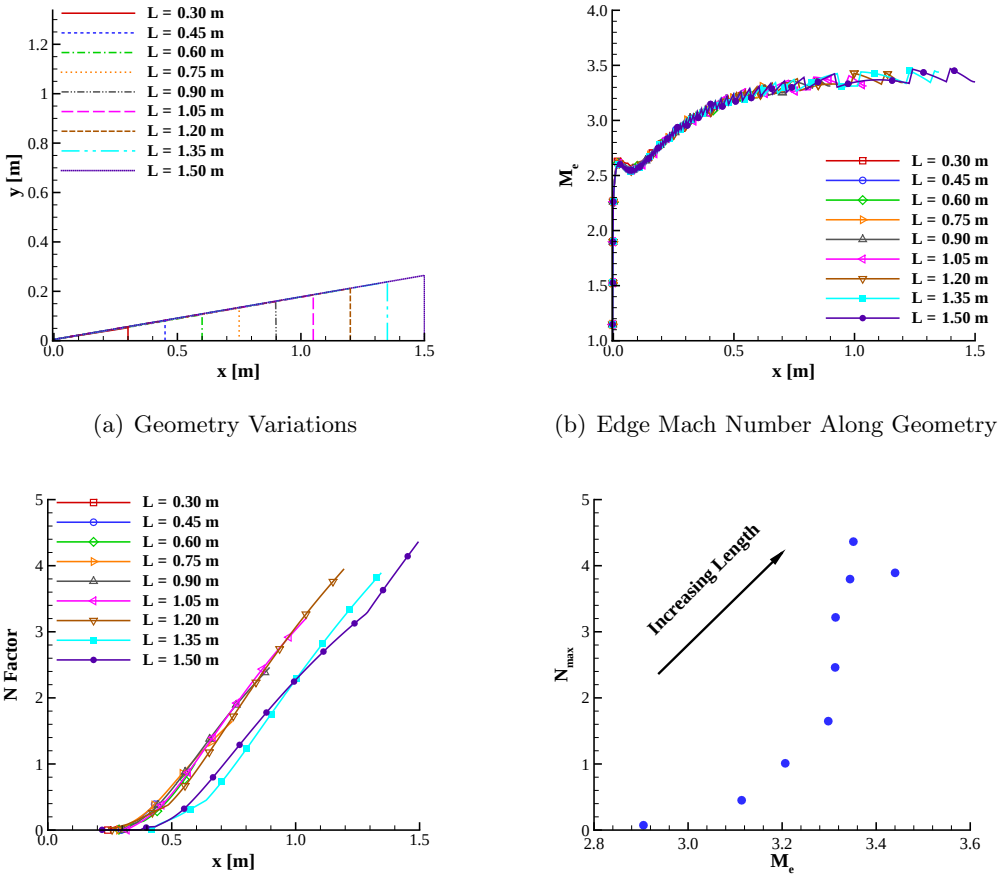

(a) Geometry Variations

(b) Edge Mach Number Along Geometry

(c) Maximum First Mode N Factors Along Geometry

(d) Trend in Maximum First Mode N Factors with Edge Mach Number at Aft End of Geometry

Figure 4.4: Length Sensitivities

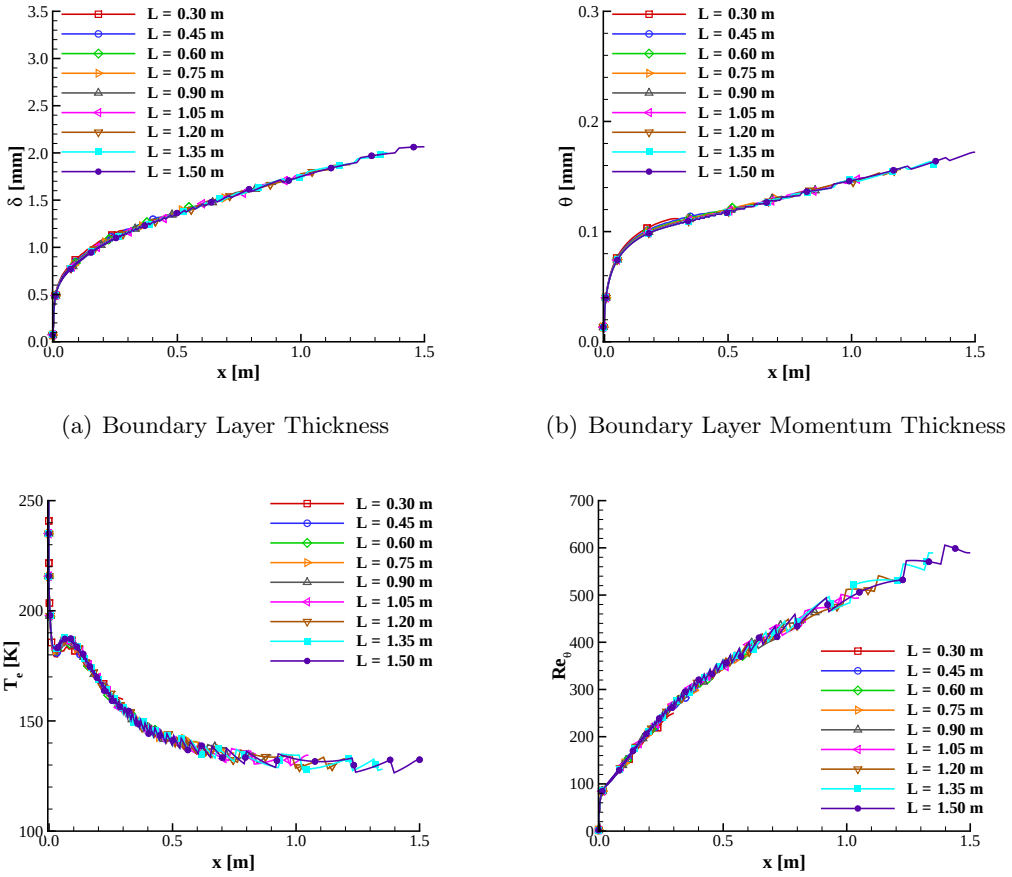

(a) Boundary Layer Thickness

(b) Boundary Layer Momentum Thickness

(c) Boundary Layer Edge Temperature

(d) Momentum Thickness Reynolds Number

Figure 4.5: Boundary Layer Properties with Changes in Vehicle Length

4.1.3 Effect of Cone Half Angle

The sensitivity of the growth of first mode instabilities to changes in the cone half angle can be seen in Figure 4.6. For this study, the surface distance of the cone was limited to approximately one meter in an attempt to isolate the effects of the changes in half angle from the changes in surface distance. As was shown in Figure 4.4(d), increasing the length, or in this case the increase in surface distance resulting from increasing the half angle, causes an increase in the maximum first mode N factors. For this reason, the cones in Figure 4.6(a) have a decreasing length in the x-direction as the cone half angle increases. Figure 4.6(d) shows changes in the maximum first mode N factor with changes in the edge Mach number at the aft end of the vehicle. The maximum first mode N factor peaks at 2.9 when the cone half angle is 20°. Increasing the half angle generally decreases the edge Mach number at the aft end of the vehicle as well as the maximum first mode N factor. However, the results from the 2° and 5° cases (labeled on the plot) do not follow this trend. The N factor curves for each geometry are seen in Figure 4.6(c) where the maximum first mode N factor curves for the 10° and 20° have the steepest slope. This means the growth rate of first mode disturbances is higher for those two half angles.

The boundary layer thickness in Figure 4.7(a) and momentum thickness in Figure 4.7(b) show that the geometries with smaller half angles have similar thickness along the body. However, as the half angle increases, the boundary layers become thinner and the edge temperature in Figure 4.7(c) also increases. The thinner boundary layers also correspond to the cases with the smallest first mode N factors. At the largest cone half angle of 45°, the edge temperature is much higher than the edge temperatures seen in any of the geometries studied in the sensitivity analysis because the edge Mach number is also the lowest seen in any of these geometries. This causes the wall-to-edge temperature ratio, T_w/T_e, to be close to 1, which is a low value, and corresponds to the case with the smallest maximum first mode N factor in this study. This also causes the value of Re_θ along the geometry, seen in Figure 4.7(d), to exceed 900 for the higher half angle case as the edge temperature increases and the viscosity at the edge of the boundary layer decreases.

In the cases with half angles higher than 20°, the maximium first mode N factors are not as large as the lower half angle geometries, but the maximum first mode N

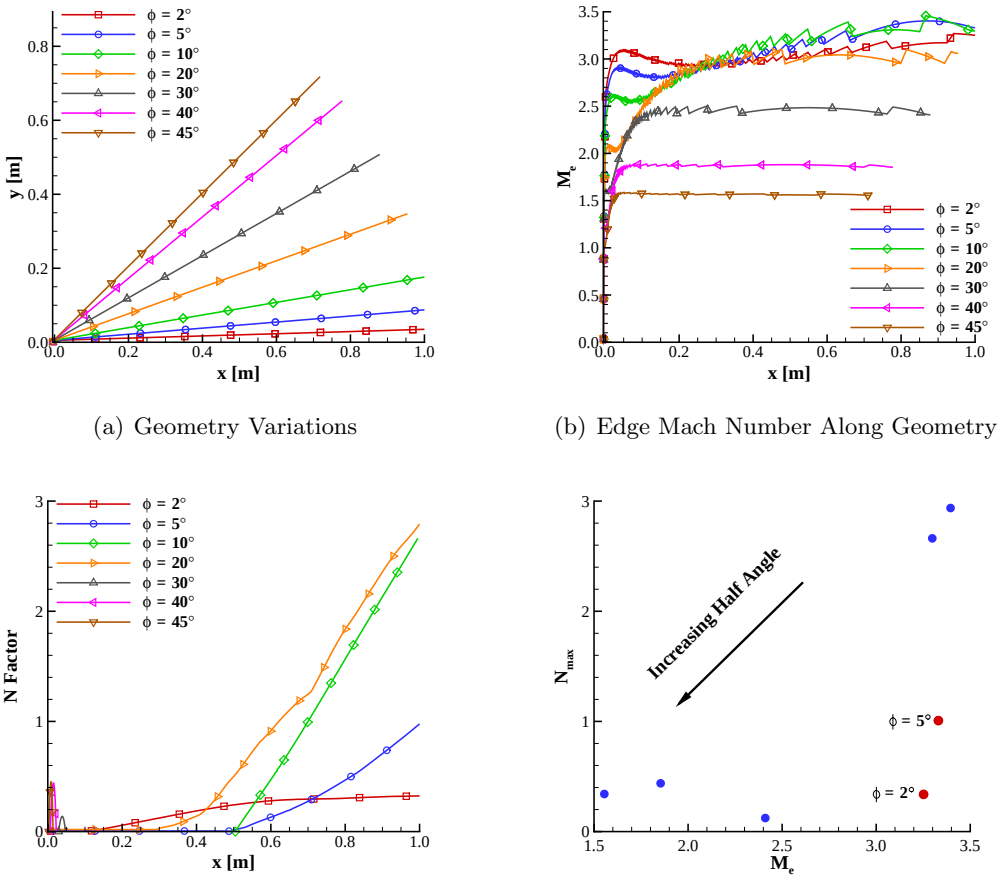

(a) Geometry Variations

(b) Edge Mach Number Along Geometry

(c) Maximum First Mode N Factors Along Geometry

(d) Trend in Maximum First Mode N Factors with Edge Mach Number at Aft End of Geometry

Figure 4.6: Cone Half Angle Sensitivities

factors for these higher half angle cases occur closer to the nose and are quickly reduced moving towards the aft of the vehicle. This behavior was also observed in the nose radius sensitivity study with the larger nose radii, so it is hypothesized that the flow in these cases is also being slowed through bluntness.

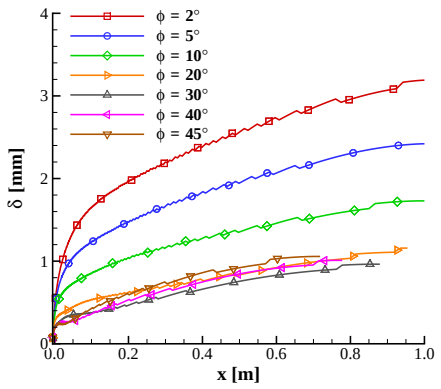

(a) Boundary Layer Thickness

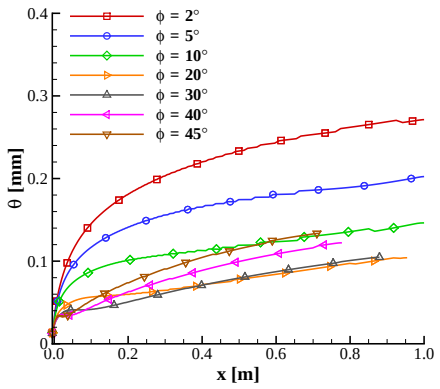

(b) Boundary Layer Momentum Thickness

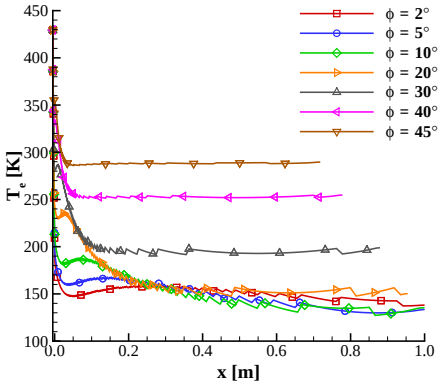

(c) Boundary Layer Edge Temperature

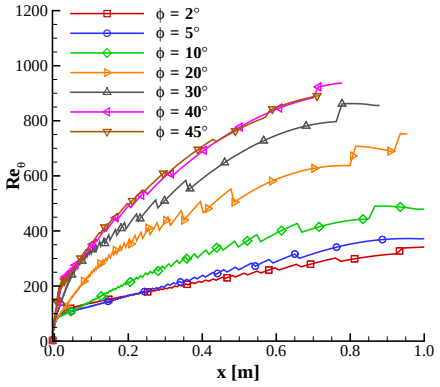

(d) Momentum Thickness Reynolds Number

Figure 4.7: Boundary Layer Properties with Changes in Cone Half Angle

4.1.4 Effect of Convex Curvature

Curvature was the next parameter examined in the sensitivity study - first convex and then concave. Figure 4.8 shows the shape of the convex and concave curvature compared to the baseline outer mold line (OML) for reference.

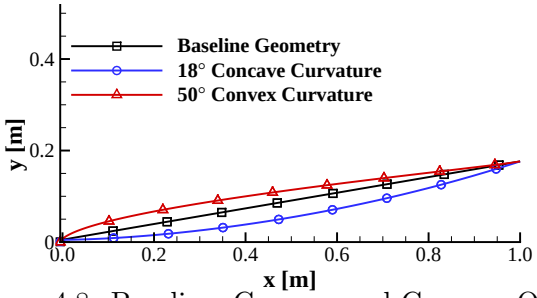

Figure 4.8: Baseline, Convex, and Concave OMLs

The convex curvature was introduced by changing the θ_1 parameter in the OML definition, and the degree of convex curvature for this sensitivity study can be seen in Figure 4.9(a). The edge Mach number along the body in Figure 4.9(b) decreases slightly as the degree of convex curvature is increased. Figure 4.9(d) shows that the maximum first mode N factor also decreases with decreasing edge Mach number, with the maximum first mode N factor being 1.9 at 10° of convex curvature. This trend is similar to that seen in the changes in nose radius because increasing the convex curvature has a similar effect on the flow to increasing the nose radius. The maximum first mode N factor curves in Figure 4.9(c) show the same trend - geometries with the least convex curvature have the largest first mode N factors and the highest growth rates compared to those geometries with higher degrees of convex curvature. Similar to the trends seen in the changes in nose radius, the boundary layer properties seen in Figure 4.10 show the boundary layer getting thicker as the convex curvature is increased. Although, close to the nose, the boundary layer grows more quickly as the convex curvature is changed than it does when the nose radius is changed, and the geometry with the highest first mode N factor, 10° of curvature, has the thinnest boundary layer. This is also consistent with the nose radius sensitivity results, but not for other sensitivity variables. The overall boundary layer and momentum thicknesses are also smaller for the case examining the changes in convex curvature.

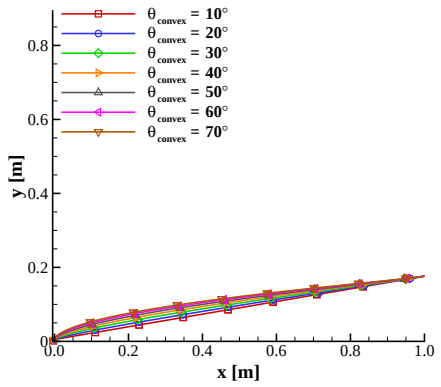

(a) Geometry Variations

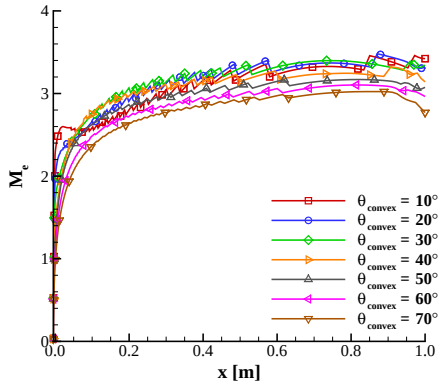

(b) Edge Mach Number Along Geometry

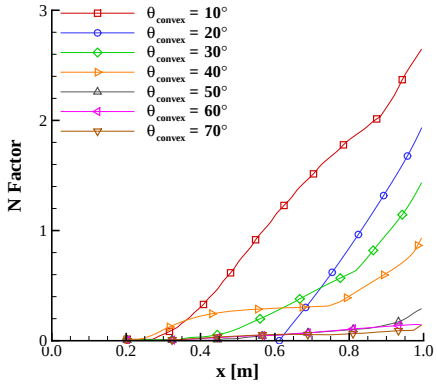

(c) Maximum First Mode N Factors Along Geometry

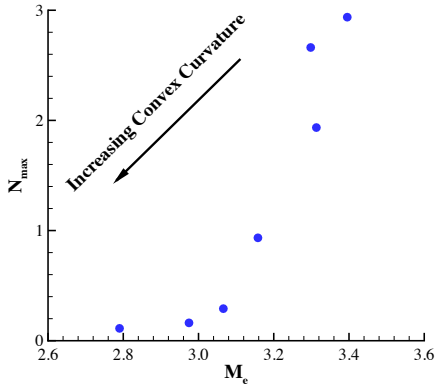

(d) Trend in Maximum Overall First Mode N Factors with Edge Mach Number at Aft End of Geometry

Figure 4.9: Convex Curvature Sensitivities

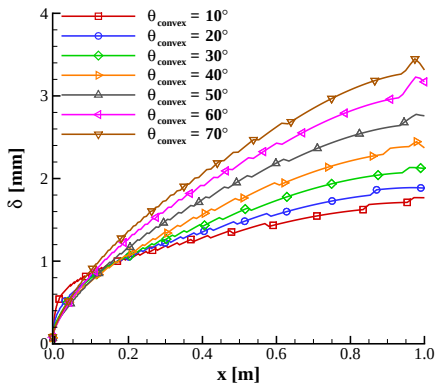

(a) Boundary Layer Thickness

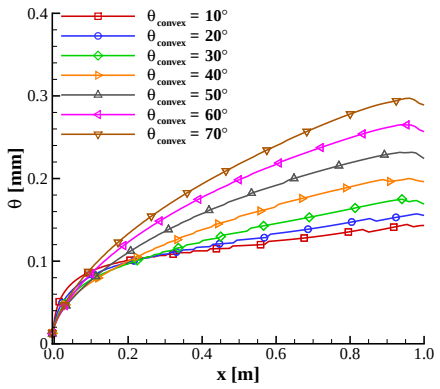

(b) Boundary Layer Momentum Thickness

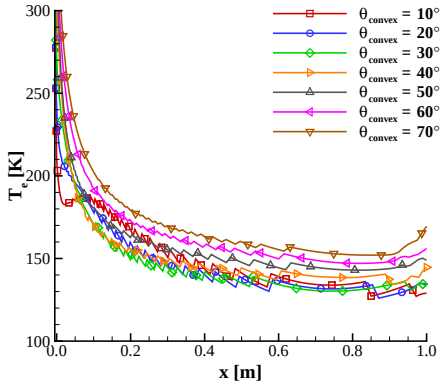

(c) Boundary Layer Edge Temperature

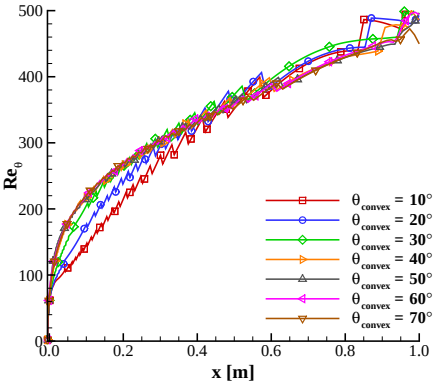

(d) Momentum Thickness Reynolds Number

Figure 4.10: Boundary Layer Properties with Changes in Convex Curvature

4.1.5 Effect of Concave Curvature

The sensitivity to concave curvature showed the largest first mode N factors of all the geometric parameters studied. The maximum first mode N factor recorded for the sensitivity to concave curvature was 7.2 for the case with 26° of curvature, the maximum studied here. The concave curvature was varied through changes in the θ_2 parameter in the OML parameterization. The sensitivity of the maximum first mode N factor to the edge Mach number at the aft end of the geometry can be seen in Figure 4.11(d) as the concave curvature is varied. In contrast to the trend seen in the other geometric parameters studied where the largest maximum first mode N factors were seen at the highest edge Mach numbers, the largest first mode N factors for the study of concave curvature resulted when the edge Mach number at the aft end of the vehicle was small. Figure 4.11(c) shows the growth rate of first mode instabilities increasing only slightly as the concave curvature is increased, but the growth of those instabilities begins sooner for the cases with higher concave curvature. Figure 4.12 also shows that the boundary layer properties along the length of the body vary in a different way than the boundary layer properties vary with changes in any of the other sensitivity parameters. In all of the cases, the boundary layer thickness and momentum thickness in Figure 4.12(a) and Figure 4.12(b), respectively, increase quickly near the nose of the vehicle. Then, depending on the degree of concave curvature, the boundary layer continues to grow if the curvature is small or gets thinner as the curvature increases and the boundary layer faces an adverse pressure gradient. The case with the highest concave curvature and largest first mode N factor also shows the thickest boundary layer near the nose and the thinnest boundary layer towards the aft. To a lesser degree, this trend is observed in the 10° convex curvature case also. When the concave curvature is large, the boundary layer at the aft end of the vehicle changes thickness at a much smaller rate and the unstable frequencies are allowed to amplify very quickly in a boundary layer that is not changing dramatically.

To further investigate the large differences in the instability seen in the concave curvature geometries, which contrasts the stability seen in the convex curvature cases, the pressure at the wall along the length of the geometry was examined. The wall pressure along the length of three geometries is compared in Figure 4.13: the baseline geometry with no surface curvature, the geometry with 70° of convex curvature, and

the geometry with 26° of concave curvature.

Looking first at the wall pressure for the baseline case, a favorable pressure gradient (one where the pressure is decreasing as the flow moves downstream) is observed near the nose. However, the pressure quickly becomes nearly constant past the nose. For this baseline case, the maximum first mode N factor observed was 2.7. Comparing this pressure distribution to that seen in the case with convex curvature, the same strongly favorable pressure gradient is observed near the nose, but moving downstream, the pressure continues to decrease. This favorable pressure gradient along the entire body corresponds to an accelerating flow and a boundary layer that is more stable than the baseline case. The maximum first mode N factor observed for the convex curvature case was 0.1, which is much lower than that for the baseline case. Finally, the geometry with concave curvature shows a very different pressure distribution than seen in the other two geometries. The strong favorable pressure gradient exists on the nose as was seen in the other two cases. However, in the concave curvature case, just past the nose, the pressure begins to increase dramatically as the flow is convected down the body and produces a strongly adverse pressure gradient. The adverse pressure gradient decelerates the flow and destabilizes the boundary layer. In this case with concave curvature, the destabilized boundary layer provided the opportunity for disturbances to amplify and the resulting maximum first mode N factor was 7.2.

With this examination, it can be seen that the wall pressure distribution can inform the stability characteristics of the boundary layer. A favorable pressure gradient will accelerate the flow and stabilize the boundary layer, and an adverse pressure gradient will slow the flow and destabilize the boundary layer allowing disturbances to amplify quickly.

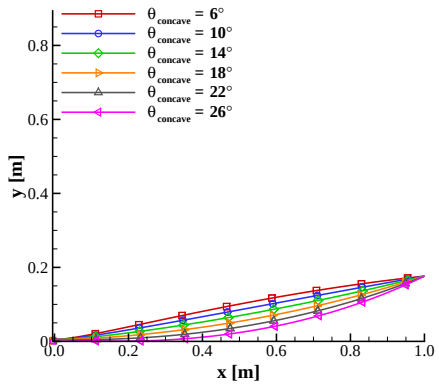

(a) Geometry Variations

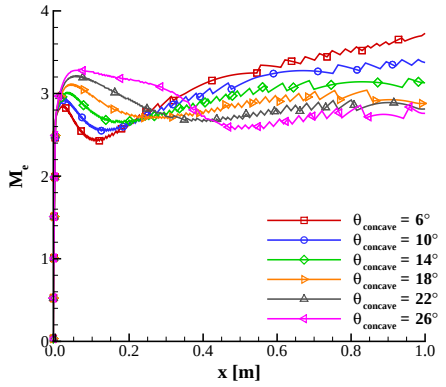

(b) Edge Mach Number Along Geometry

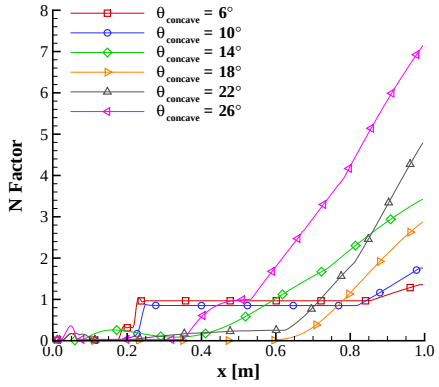

(c) Maximum First Mode N Factors Along Geometry

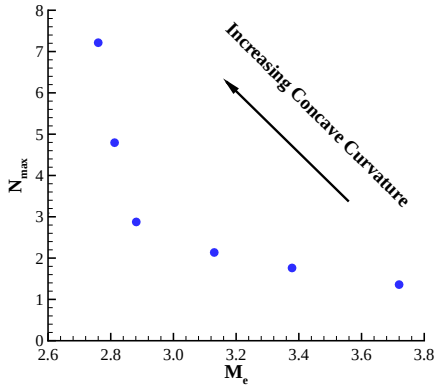

(d) Trend in Maximum Overall First Mode N Factors with Edge Mach Number at Aft End of Geometry

Figure 4.11: Concave Curvature Sensitivities

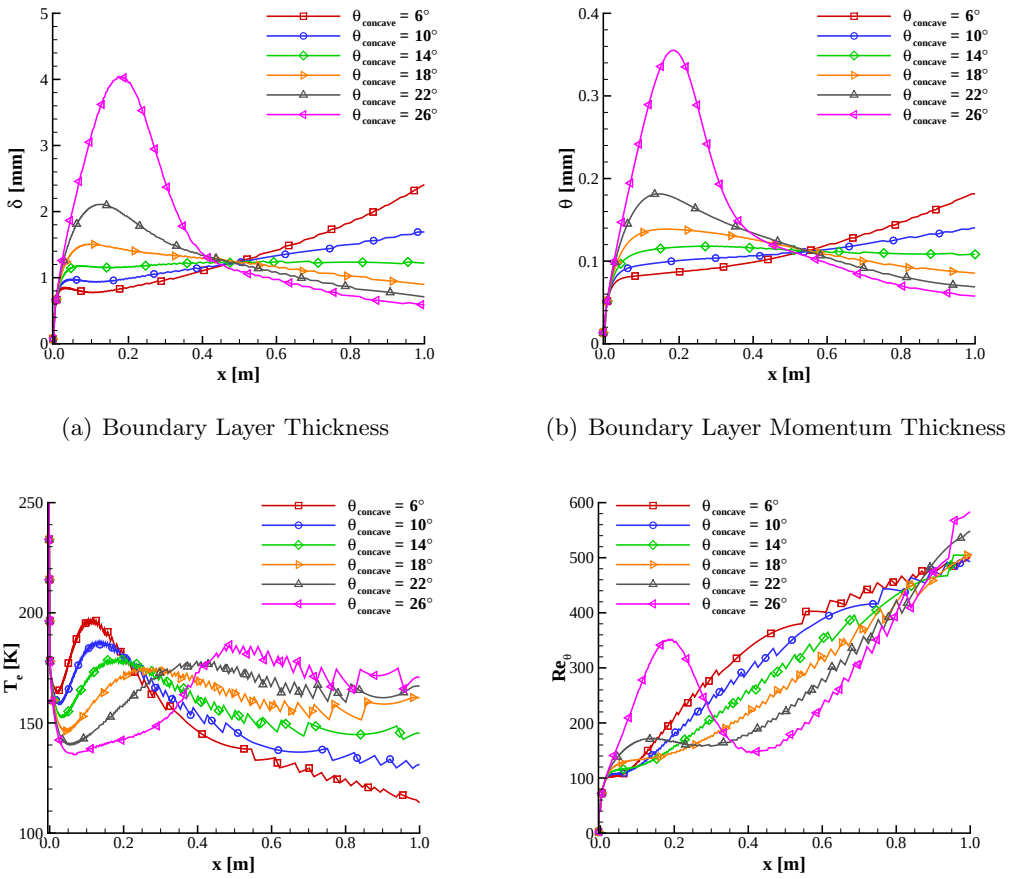

(a) Boundary Layer Thickness

(b) Boundary Layer Momentum Thickness

(c) Boundary Layer Edge Temperature

(d) Momentum Thickness Reynolds Number

Figure 4.12: Boundary Layer Properties with Changes in Concave Curvature

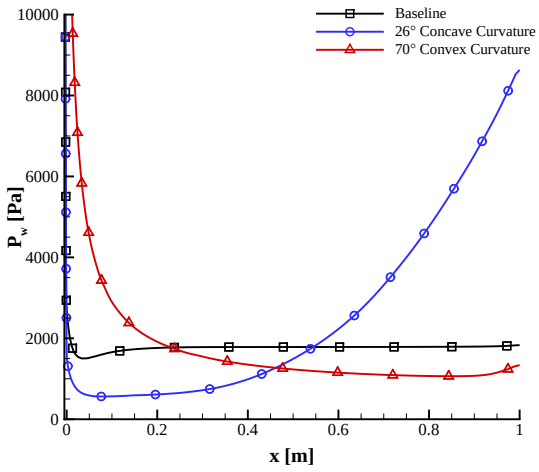

Figure 4.13: Wall pressure distribution for baseline geometry with no curvature, geometry with 70° of convex curvature, and geometry with 26° of concave curvature.

4.1.6 Composite Geometry

The results of the sensitivity analysis were combined into a single, composite geometry to determine if the amplification of first mode waves could be increased. The geometry configuration from each sensitivity analysis that produced the largest first mode N factors was chosen for the composite geometry. This resulted in the geometry shown in Figure 4.14 with the geometric parameters in Table 4.2.

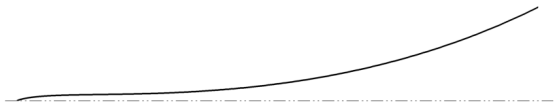

Figure 4.14: Geometry for Composite Sensitivity Analysis

Table 4.2: Geometric Parameters for Composite Geometry

Geometric Parameter	Value
Nose Radius [mm]	1.0
Length [m]	1.5
Half Angle [°]	10.0
Concave Curvature [°]	26.0
Convex Curvature [°]	20.0

A boundary layer stability analysis was performed and the maximum first mode N factors that resulted can be seen in Figure 4.16(a). The edge Mach number at the aft end of the vehicle was 2.9. The maximum boundary layer velocity thickness of 2.3 mm was observed near the nose of the vehicle and decreased quickly towards the aft of the geometry where the concave curvature compresses the boundary layer. The distribution of the velocity, displacement, and momentum thicknesses can be seen in Figure 4.15. This peak in the boundary layer thickness, seen also in the convave geometry sensitivity analysis, is also observed in the displacement and momentum thicknesses for the composite geometry, but to a lesser degree.

Several first mode frequencies were amplified in the boundary layer for this geometry, and the maximum first mode N factor was 8.2. This was larger than any first mode N

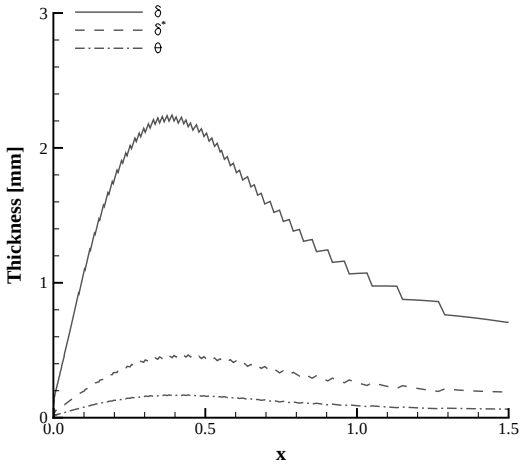

Figure 4.15: Boundary Layer Velocity, Displacement, and Momentum Thicknesses for Composite Geometry

factor seen when each of the parameters was studied individually. However, examining the overall maximum N factors in Figure 4.16(b), which includes second mode instabilities, large second mode N factors were observed half way down the geometry. The second mode N factors are distinguished from the first mode N factors by the higher disturbance frequencies closer to the second mode frequency predicted by STABL. The amplification of second mode instabilities in this case would likely cause transition in a test facility before the first mode instabilities were able to grow large enough to cause transition. For this reason, the optimization to minimize second mode instabilities while maximizing first mode instabilities was desired.

In the sensitivity analysis conducted here, second mode instabilities were not considered or recorded. As a result, many of the geometries evaluated in this analysis may be dominated by second mode instabilities as was seen in the composite geometry above. If second mode instabilities were evaluated and N factors calculated, the overall maximum N factor may be larger than the values of maximum first mode N factor reported here. If any of these geometries were to be tested, boundary layer transition may be the result of second mode instabilities if second mode disturbances are more amplified than first

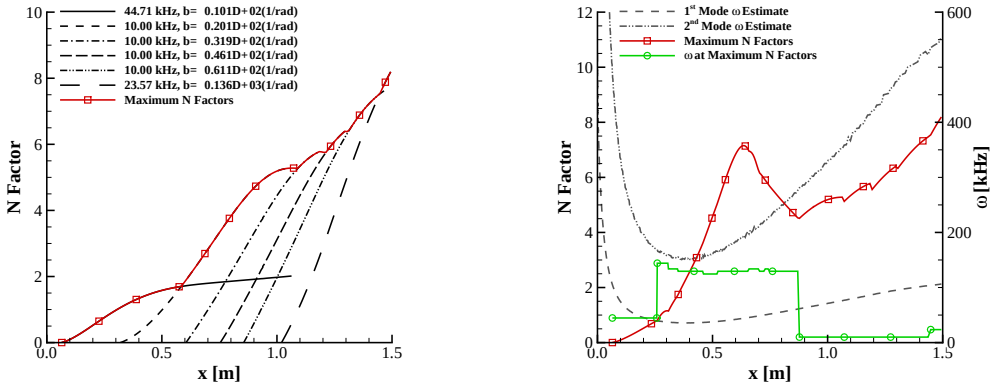

(a) First Mode N Factor Curves

(b) Overall Maximum N Factor and Disturbance Frequency

Figure 4.16: Stability Results for Compiled Geometry

mode disturbances. Also, this 2D analysis did not take into account any non-parallel effects such as the interaction of instability modes or three-dimensional effects such as Göertler instabilities that would likely develop on any geometry with concave curvature. These effects would need to be considered in any flight vehicle or ground test article design.

4.1.7 Effects of Wall Temperature

In addition to showing the increase in amplification of first mode instabilities that resulted from creating a composite geometry, the effects of changes in wall temperature were also investigated. Changes in wall temperature have been shown to have a strong effect on the growth of first mode waves. The composite geometry from the sensitivity analysis was chosen for this analysis because both first and second mode instabilities dominated the boundary layer flow at different points along the geometry, as was evident in Figure 4.16. Three additional wall temperatures were chosen to determine how the amplification of first and second mode instabilities changed as the wall temperature was increased or decreased. Isothermal wall conditions at ±50 K from the baseline 300 K wall temperature case were analyzed along with an adiabatic wall case. Figure 4.17 shows the results of this study with N factors shown in solid lines with symbols on the

left y-axis and the corresponding disturbance frequency in dashed lines with symbols on the right y-axis. The predicted first and second mode frequencies are also shown for reference.

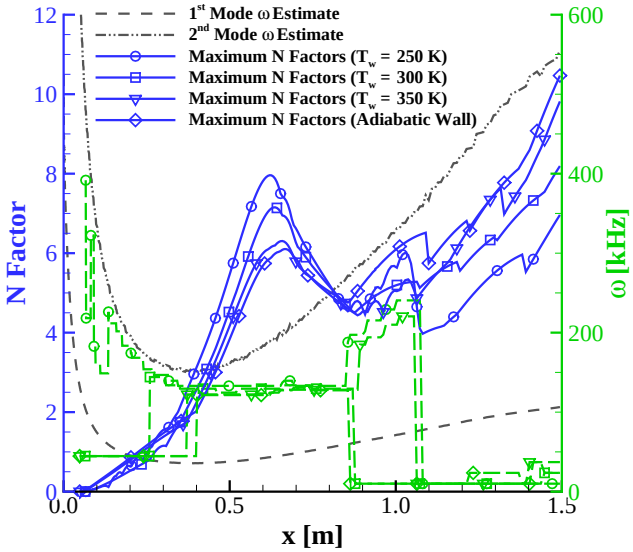

Figure 4.17: Maximum N Factors and Corresponding Disturbance Frequencies for Wall Temperature Study

Decreasing the wall temperature to 250 K at these freestream conditions showed an increase in the growth rate of second mode disturbances and a decrease in the growth rate of first mode disturbances. Additionally, a smaller secondary peak in the second mode N factor, which was not present in the baseline case, appears downstream of the primary peak. The disturbance frequencies in this case also appear to follow the second mode predictions more closely near the nose of the geometry than the other cases in this study.

As the wall temperature is increased above the baseline case to 350 K, the first mode N factor at the aft end of the vehicle increases above that seen in the baseline case and the primary peak in the second mode N factor decreases. These trends are consistent with trends seen by other researchers. However, the stability analysis in this case also shows a secondary peak in the second mode N factor that was not present in the baseline case. The secondary peak has a smaller amplitude than that seen in the case with a wall temperature of 250 K, but it is unclear why this peak appears in these two cases, but not the baseline case.

Finally, the wall was allowed to reach an adiabatic condition that would provide a natural upper bound on the achievable wall temperature in a long duration test facility or flight environments. The stability analysis results again showed an increase in the maximum first mode N factor at the aft end of the vehicle and a reduction in the maximum second mode N factor seen near the middle of the vehicle. This case showed no secondary peak in the second mode N factor.

The edge temperature and edge Mach number distributions along the geometry remained the same for all cases, but the wall-to-total temperature ratio, T_w/T_0, changed as the wall temperature changed. Table 4.3 shows the variation in the temperature ratio for the specified wall temperature conditions.

Table 4.3: Wall-to-Total Temperature Ratios for Composite Geometry at Aft of Geometry

T_w [K]	T_w/T_0
250.0	0.58
300.0	0.69
350.0	0.81
378.2 (Adiabatic)	0.88

The trends in amplification of first and second mode waves with changes in wall temperature seen in this study are consistent with the results seen in the literature.[7] As the wall temperature is decreased, the first mode waves are stabilized and second mode waves are destabilized. As the wall temperature is increased, the opposite is true and the first mode waves grow at faster rate while the second mode waves are stabilized. Although these results show that increasing the wall to total temperature ratio has the desired effect of increasing the amplification of the first mode waves, the wall temperature would likely have to be heated far above adiabatic temperatures to completely eliminate the growth of second mode waves. However, the increase in wall temperature did increase the amplification of first mode waves enough that it may be possible to measure these instability waves on this geometry at these freestream conditions. This study also shows that the wall temperature is an important parameter that can be used in the experimental setting for simultaneously increasing the amplification of first mode instabilities while decreasing the amplification of second mode instabilities.

4.2 Optimization

The optimization portion of this study was conducted in two pieces since the edge Mach number can be lowered through an oblique shock or due to nose bluntness. To accommodate this, two optimization analyses were set up with different bounding parameters: one that limited the geometry to a sharp, slender cone geometry that would lower the edge Mach number through an oblique shock, and one that limited the geometry to a blunter shape that would lower the edge Mach number due to nose bluntness. In the optimization process, the freestream conditions were held constant at the Mach 6 conditions shown in Table 3.2 and the OML was parameterized as described in Section 3.2.

4.2.1 Slender Body Optimization

For the optimization of a slender body that would lower the edge Mach number through an oblique shock, the optimization bounds on the geometric parameters were limited to those seen in Table 4.4.

Table 4.4: Geometric Bounds for Slender Body Optimization

Geometric Parameter	Minimum	Maximum
Nose Radius [mm]	0.5	10.0
Length [m]	0.5	2.0
Half Angle [°]	2.0	10.0
Concave Curvature [°]	0.0	10.0
Convex Curvature [°]	0.0	70.0

The resulting optimized slender geometry was a cone with a small half angle, a small flare at the aft end, and a slight convex curvature near the nose. The resulting geometry can be seen in Figure 4.18 and the tabulated geometric parameters can be found in Table 4.5.

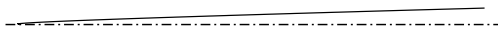

Figure 4.18: Geometry for Optimized Slender Body

Table 4.5: Geometric Parameters for Optimized Slender Body

Geometric Parameter	Value
Nose Radius [mm]	0.5
Length [m]	0.5
Half Angle [°]	2.0
Concave Curvature [°]	4.7
Convex Curvature [°]	16.9

The stability analysis resulted in a maximum first mode N factor of 2.85 at the aft end of the geometry. Figure 4.19(a) shows each of the amplified first mode frequencies

with the maximum first mode N factor curve shown with symbols. The maximum second mode N factor reached was 1.87 at x = 0.35 meters and after this point, no other second mode disturbances are observed. The stability results showing both first and second mode N factor curves can be seen in Figure 4.19(b). With the exception of the few locations where the second mode disturbances are more amplified than the first mode disturbances for short distances, the boundary layer for this geometry appears to be mostly dominated by first mode instabilities.

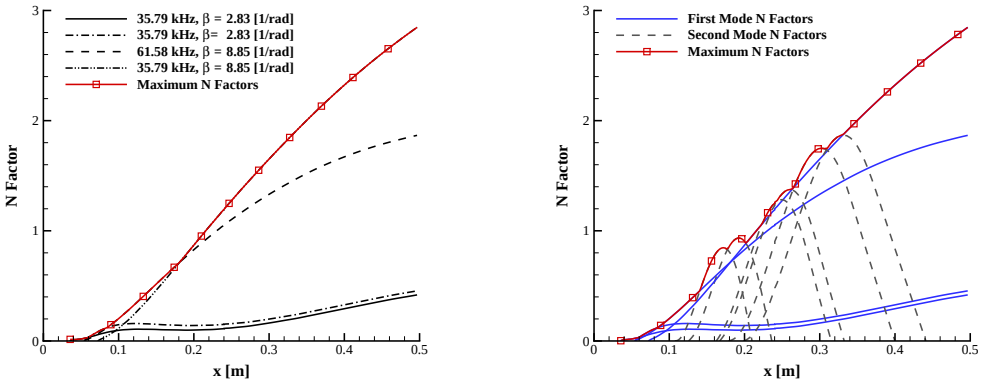

(a) First Mode Only

(b) First and Second Mode

Figure 4.19: N Factors for Slender Optimized Geometry

The edge Mach number at the aft end of this geometry was 3.8, which was on the higher end of the edge Mach numbers extracted during the sensitivity analysis, and the velocity, displacement, and momentum thicknesses of the boundary layer along the geometry are found in Figure 4.20. At the aft end, the boundary layer thicknesses were 2.36 mm, 0.45 mm, and 0.13 mm, respectively, which were on the low end of those thicknesses observed in the sensitivity analysis.

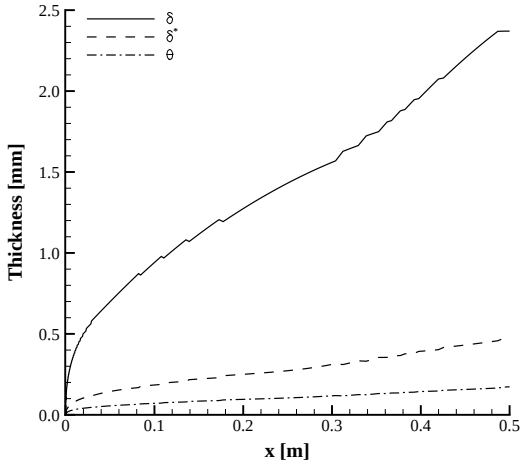

Figure 4.20: Boundary Layer Velocity, Displacement, and Momentum Thicknesses for Slender Optimized Geometry

With the small nose radius, small cone half angle, and small degree of convex curvature, these results follow the same trends seen in the sensitivity analysis in Section 4.1. However, the short length of the vehicle does not follow the trend seen previously. With the stability analysis showing that the second mode disturbances are no longer amplified after x = 0.35 meters, it would seem that a longer geometry would allow the first mode disturbances being amplified and continue to grow reaching higher N factors than observed here. This phenomenon should be investigated further to understand why the geometry was optimized to such a short length. Also of note, the values of the parameters composing this optimized slender body geometry fall at or very near the minimum bounds of the optimization, and this may be affecting the results seen here.

4.2.2 Blunt Body Optimization

For the blunt body optimization, the geometry was bounded by the parameters in Table 4.6. These bounds were chosen to optimize a geometry that would slow the flow due to bluntness instead of through an oblique shock, and therefore, bounded the optimization space on the lower end with a larger nose radius and larger cone half angle than were allowed for the slender body optimization.

Table 4.6: Geometric Bounds for Blunt Body Optimization

Geometric Parameter	Minimum	Maximum
Nose Radius [mm]	10.0	500.0
Length [m]	0.5	2.0
Half Angle [°]	10.0	50.0
Concave Curvature [°]	0.0	30.0
Convex Curvature [°]	0.0	70.0

Figure 4.21 shows the optimized blunt body with a large nose radius and very little surface curvature. The corresponding optimized parameters can be found in Table 4.7.

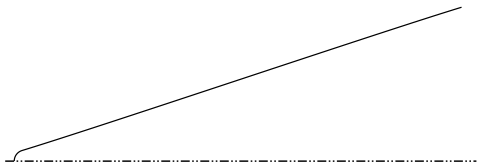

Figure 4.21: Geometry for Optimized Blunt Body

The stability analysis for the optimized blunt body geometry showed several unstable first mode frequencies, and their integrated growth rates are shown in Figure 4.22. The maximum first mode N factor was 2.79 at the aft end of the vehicle and no unstable second mode disturbances were observed.

The edge Mach number at the aft end of the blunt optimized geometry was 2.61, which was on the lower end of the edge Mach numbers seen in the sensitivity analysis,

Table 4.7: Geometric Parameters for Optimized Blunt Body

Geometric Parameter	Value
Nose Radius [mm]	25.1
Length [m]	0.99
Half Angle [°]	19.4
Concave Curvature [°]	16.9
Convex Curvature [°]	17.5

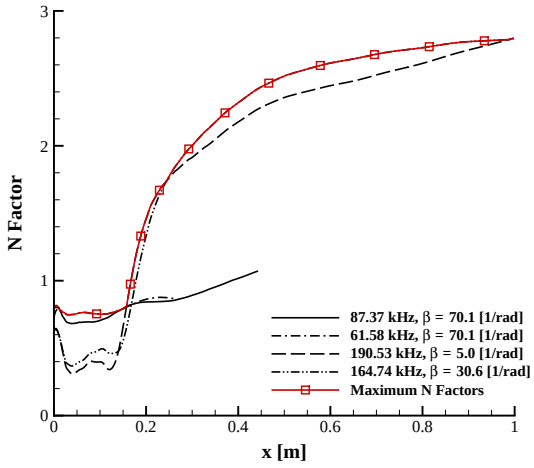

Figure 4.22: First Mode N Factors for Blunt Optimized Geometry

and the boundary layer velocity, displacement, and momentum boundary layer thicknesses at the aft end of the geometry were 1.75 mm, 0.46 mm, and 0.17 mm, respectively. The distributions of these values along the geometry are shown in Figure 4.23.

In the nose radius sensitivity analysis, nose radii above 30 mm showed amplification of first mode waves near the nose of the vehicle, which is believed to be due to the flow slowing from bluntness as opposed to through an oblique shock. The optimized geometry for this blunt case resulted in a nose radius that was smaller than that 30 mm threshold seen in the sensitivity analysis, so the flow may slowed by an oblique shock in this case as well. However, the cone half angle is near 20°, which was shown in the half angle sensitivity analysis to produce the largest first mode N factors.

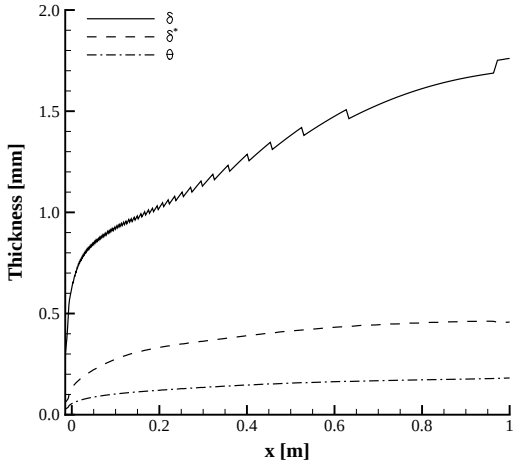

Figure 4.23: Boundary Layer Velocity, Displacement, and Momentum Thicknesses for Blunt Optimized Geometry

An interesting result in both the slender optimzed geomerty and blunt optimized geometry is the lack of significant surface curvature. The sensitivity results from the convex curvature and concave curvature analyses showed first mode N factors reaching far higher than those seen in either optimized case. This may be a result of the initial conditions chosen for these optimization cases where no surface curvature was specified. Since the gradient-based optimization algorithm used here is very dependent on the initial conditions, future analysis may include changes in the optimization algorithm or changes in the initial conditions that investigate the introduction of surface curvature in the initial conditions.

Chapter 5

Conclusions and Discussion

The work presented here examined the effects of geometric changes to an axisymmetric cone on the amplification of first mode instability waves. Constant Mach 6 freestream conditions were used with a constant wall temperature, and the geometric parameters varied were the nose radius, length, cone half angle, degree of convex curvature, and degree of concave curvature. A sensitivity analysis was performed to determine the changes in maximum first mode N factor as each of the geometric parameters was varied individually. Boundary layer properties such as thickness, momentum thickness, edge Mach number, and edge temperature were also recorded. Results of the sensitivity analysis showed that cones with small nose radii at these conditions had large first mode N factors near 6 at the aft end of the vehicle, but the first mode N factors were largest near the nose for cones with large nose radii. The maximum first mode N factors were also much smaller for the large nose radii than for the small nose radii. Increasing the length of the geometry allowed disturbances a longer length to grow, so as the length increased, the maximum first mode N factor increased to a maximum value of 4.5. The maximum first mode N factors resulting from changes in the cone half angle were small for very small half angles and very large half angles. The largest first mode N factor of 2.9 was found at half angles of 10° and 20°. Analysis of the convex curvature showed that increasing the convex curvature decreased the maximum first mode N factors, and the largest first mode N factor was 1.9. The largest effect on first mode N factors was seen by increasing the concave curvature of the cone. A maximum first mode N factor of 7.2 was seen with 26° of concave curvature, and first mode N factors decreased quickly

as the concave curvature was decreased.

In general, the largest maximum first mode N factors occurred when the edge Mach number at the aft end of the vehicle was largest, and the maximum first mode N factor decreased as the edge Mach number at the aft end of the vehicle decreased, approximately parabolically. However, the effects of changes in the concave curvature resulted in a trend in maximum first mode N factors and edge Mach numbers that was opposite that of the other parameters with the largest first mode N factor occurring at the lowest edge Mach number at the aft end of the vehicle. The largest edge Mach numbers at the aft end of the vehicle seen in this study were near 3.5. In all of the sensitivity analyses, the geometry that produced the largest first mode N factors had the one of the thinnest boundary layers when compared to other geometries in the same study. In the concave curvature study, though, the geometry with the highest degree of curvature that produced the largest first mode N factors had a large increase in the boundary layer thickness near the nose before the boundary layer thinned near the aft of the vehicle. This was also seen in the convex curvature study to a much lesser degree, but was not observed in any other sensitivity parameter.

Combining the results of the sensitivity analysis into a composite geometry composed of parameters that produced the largest first mode N factors in the individual analyses resulted in the largest first mode N factors recorded in the study. This composite geometry had a small nose radius and a large flare from a large degree of concave curvature. The maximum first mode N factor for the composite geometry was 8.2, but large second mode N factors near 7 were seen upstream on the vehicle and may cause transition in a test facility before the first mode instabilities were able to grow. An investigation into the effects of changes in wall temperature on the composite geometry showed that increasing the wall temperature, and therefore the wall-to-total temperature ratio, reduced the amplification of instabilities at second mode frequencies and increased the amplification of instabilities at first mode frequencies. The adiabatic wall temperature was the highest wall temperature examined provided a 30% increase in the maximum first mode N factor recorded at the aft end of the geometry. However, at these flow conditions on this geometry, the maximum second mode N factor was still large enough that transition due to second mode instabilities may occur before the first mode instabilities could grow large enough to be measured or cause transition. Increasing the

wall temperature well above adiabatic may be required to eliminate the second mode amplification or at least reduce it enough for the first mode instabilities to dominate the flow.

Two geometries were optimized by allowing all the geometric sensitivity parameters to vary simultaneously. The first, a slender geometry designed to slow the flow through an oblique shock, was optimized to a very short slender cone with a sharp nose radius. The first mode disturbances dominated most of the flow down the length of the body, and the second mode disturbances were no longer amplified just beyond half way down the length. The short length of 0.5 meter, however, was not expected since the length sensitivity analysis showed that longer vehicles allow the disturbances to amplify more than short vehicles. The maximum first mode N factor, 1.87, was also much lower than expected for an optimized geometry. The second geometry, a blunt cone with a large half angle resulted from an optimization designed to create a geometry that slows the flow through bluntness. This case had a nose radius less than that shown in the nose radius sensitivity analysis to slow the flow through bluntness and a half angle less than that shown in the half angle sensitivity to slow the flow through bluntness. As a result, this blunt optimized geometry is showing behavior similar to those geometries that slowed the flow through an oblique shock. The lack of surface curvature in both geometries was surpising given the results in the sensitivity analyses that showed larger first mode N factors could result from surface curvature, especially concave curvature.

The methods used in the analyses here have their limitations. The 2D boundary layer stability analysis tool used for determining the amplification of the first and second mode instabilities does not account for any nonlinear effects or the interaction of modes, and 3D effects such as Göertler and crossflow instabilities cannot be modeled. In geometries with high degrees of concave curvature, Göertler instabilities could cause transition before any first mode instabilities were able to amplify enough to be measured. The gradient-based optimization algorithm used in the optimization analyses is known to be flawed in cases where local minima and maxima may exist in addition to the global minimum or maximum being sought. As a result, these methods are very dependent on the initial conditions.

5.1 Future Work

Building on the work presented here, future work would include an additional sensitivity analysis and further optimization analyses. The sensitivity analysis would isolate the effects of changes in nose radius from the effects of changes in cone half angle. Keeping the base radius constant while increasing the nose radius in the sensitivity analysis presented here resulted in reductions in the cone half angle. The corrected sensitivity analysis would adjust the base radius to maintain a constant half angle as the nose radius increased.

The two geometries optimized in this study both produced very small first mode N factors. If these geometries were used in an experiment, the first mode instabilities would likely be hard to measure because of the small amplification. Further optimization may include changes to the objective function to weight each of the parameters differently. Future optimization analysis could also explore other optimization algorithms that are less sensitive to initial conditions and are able to find global minima and maxima more efficiently.

Finally, this methodology could be expanded to other geometries, including three dimensional geometries, as well as different flow conditions. Expanding to three dimensional geometries and taking advantage of three dimensional tools would allow for other instability mechanisms to be considered, as well as possibly non-parallel effects and the interaction of different instability modes. In this way, this method could be applied to test article design to maximize the amplification of first mode instabilities to be able to measure them and study them in ground test facilities. This method may also be able to optimize a test article or flight vehicle to delay transition to assist in thermal protection system mass reduction or inconsistencies in vehicle controllability as the boundary layer transitions from laminar to turbulent.

References

[1] Stetson, K., "On Predicting Hypersonic Boundary Layer Transition," *Air Force Wright Aeronautical Laboratories Technical Memo*, AFWAL-TM-87-160-FIMG, March 1987.

[2] Alba, C., Casper, K., Beresh, S., Schneider, S., "Comparison of Experimentally Measured and Computed Second-Mode Disturbances in Hypersonic Boundary-Layers," *48th AIAA Aerospace Sciences Meeting*, AIAA Paper 2010-897, January 2010.

[3] Wadhams, T., MacLean, M., Holden, M., "Recent Experimental Studies of High Speed Boundary Layer Transition in LENS Facilities to Further the Development of Predictive Tools for Boundary Layer Transition in Flight," *50th AIAA Aerospace Sciences Meeting*, AIAA Paper 2012-0470, January 2012.

[4] Wadhams, T., MacLean, M., Holden, M., "Continuing Experimental Studies of High Speed Boundary Layer Transition in LENS Facilities to Further the Development of Predictive Tools for Boundary Layer Transition in Flight," *51st AIAA Aerospace Sciences Meeting*, AIAA Paper 2013-0379, January 2013.

[5] Berridge, D., Casper, K., Rufer, S., Alba, C., Lewis, D., Beresh, S., Schneider, S., "Measurements and Computations of Second-Mode Instability Waves in Three Hypersonic Wind Tunnels," *40th AIAA Fluid Dynamics Conference and Exhibit*, AIAA Paper 2010-5002, July 2010.

[6] Alba, C., Johnson, H., Candler, G., "Oblique Wave Disturbance Analysis of Supersonic Flow Past Axisymmetric and 2D Bodies at Angles of Attack," *38th AIAA Fluid Dynamics Conference and Exhibit*, AIAA Paper 2008-4396, June 2008.

[7] Stetson, K., Kimmel, R., "On Hypersonic Boundary-Layer Stability," *30th AIAA Aerospace Sciences Meeting and Exhibit*, AIAA Paper 92-0737, January 1992.

[8] Schneider, S., "Design of a Mach-6 Quiet-Flow Wind-Tunnel Nozzle using the e**N Method for Transition Estimation," *36th AIAA Aerospace Sciences Meeting and Exhibit*, AIAA Paper 98-0547, 1998.

[9] Blanchard, A., Selby, G., "An Experimental Investigation of Wall-Cooling Effects on Hypersonic Boundary-Layer Stability in a Quiet Wind Tunnel," *NASA Contractor Report*, No. 198287, 1996.

[10] Herbert, T. "Parabolized Stability Equations," *Annual Review of Fluid Mechanics*, Vol. 29, p245-283, 1997.

[11] Johnson, H., Candler, G., "Hypersonic Boundary Layer Stability Analysis Using PSE-Chem," *35th AIAA Fluid Dynamics Conference and Exhibit*, AIAA Paper 2005-5023, June 2005.

[12] Johnson, H., "Thermochemical Interactions in Hypersonic Boundary Layer Stability," *The University of Minnesota*, July 2000.

[13] Johnson, H., Alba, C., Bartkowicz, M., Drayna, T., Candler, G., "Design Optimization of Hypersonic Vehicles for Boundary-Layer Stability," *26th AIAA Applied Aerodynamics Conference*, AIAA Paper 2008-6221, August 2008.

[14] Nompelis, I., Drayna, T., Candler, G., "Development of a Hybrid Unstructured Implicit Solver for the Simulation of Reacting Flow Over Complex Geometries," *34th AIAA Fluid Dynamics Conference and Exhibit*, AIAA Paper 2004-2227, June 2004.

[15] Adams, B.M., Bohnhoff, W.J., Dalbey, K.R., Eddy, J.P., Eldred, M.S., Gay, D.M., Haskell, K., Hough, P.D., and Swiler, L.P., "DAKOTA, A Multilevel Parallel Object-Oriented Framework for Design Optimization, Parameter Estimation, Uncertainty Quantification, and Sensitivity Analysis: Version 5.0 User's Manual," *Sandia Technical Report* SAND2010-2183, December 2009. Updated December 2010 (Version 5.1) Updated November 2011 (Version 5.2).

Appendix A

Acronyms

Table A.1: Acronyms

Acronym	Meaning
2D	Two Dimensional
3D	Three Dimensional
DAKOTA	Design Analysis Kit for Optimization and Terascale Applications
DPLR	Data Parallel Line Relaxation
LST	Linear Stability Theory
OF	Objective Function
OML	Outer Mold Line
PSE	Parabolized Stability Equations
STABL	Stability and Transition Analysis for Hypersonic Boundary Layers
TPS	Thermal Protection System